Available online at www.sciencedirect.com

ScienceDirect

www.elsevier.com/locate/jes

JES JOURNAL OF ENVIRONMENTAL SCIENCES

www.jesc.ac.cn

Comparison of activated carbon and iron/cerium modified activated carbon to remove methylene blue from wastewater

Song Cheng, Libo Zhang, Aiyuan Ma, Hongying Xia, Jinhui Peng, Chunyang Li, Jianhua Shu*

State Key Laboratory of Complex Nonferrous Metal Resources Clean Utilization, Kunming University of Science and Technology, 650093, China
Yunnan Provincial Key Laboratory of Intensification Metallurgy, Kunming University of Science and Technology, Kunming, 650093, China
National Local Joint Laboratory of Engineering Application of Microwave Energy and Equipment Technology, Kunming, 650093, China
Faculty of Metallurgical and Energy Engineering, Kunming University of Science and Technology, Kunming 650093, China

ARTICLE INFO

Article history:
Received 19 September 2016
Revised 26 November 2016
Accepted 17 December 2016
Available online 3 April 2017

Keywords:
Fe–Ce-AC
Methylene blue
Adsorption
Wastewater

ABSTRACT

The methylene blue (MB) removal abilities of raw activated carbon and iron/cerium modified raw activated carbon (Fe–Ce-AC) by adsorption were researched and compared. The characteristics of Fe–Ce-AC were examined by N_2 adsorption, zeta potential measurement, FTIR, Raman, XRD, XPS, SEM and EDS. After modification, the following phenomena occurred: The BET surface area, average pore diameter and total pore volume decreased; the degree of graphitization also decreased. Moreover, the presence of Fe_3O_4 led to Fe–Ce-AC having magnetic properties, which makes it easy to separate from dye wastewater in an external magnetic field and subsequently recycle. In addition, the equilibrium isotherms and kinetics of MB adsorption on raw activated carbon and Fe–Ce-AC were systematically examined. The equilibrium adsorption data indicated that the adsorption behavior followed the Langmuir isotherm, and the pseudo-second-order model matched the kinetic data well. Compared with raw activated carbon, the maximum monolayer adsorption capacity of Fe–Ce-AC increased by 27.31%. According to the experimental results, Fe–Ce-AC can be used as an effective adsorbent for the removal of MB from dye wastewater.

Introduction

Dyes are coloring agents used by a variety of industries, including textile, plastics, paper and pulp, to colorize their final products. A total of 30% of the world production of dyes may be lost during the dyeing process (Nethaji and Sivasamy, 2011). However, most dyes are toxic. The uncontrolled release of dye residues as industrial wastewater into receiving water streams has led to a number of negative impacts, including a decrease in light penetration as well as carcinogenic and mutagenic changes to organisms (Ghaedi et al., 2015). The dye wastewater can also cause allergies, dermatitis, and skin irritation, and induce cancer and mutations in humans (Ghaedi et al., 2013a; Mirzaei et al., 2013; Rosenkranz et al., 2007). Therefore, wastewaters with large dye contents must be treated before discharge into the environment, so as to minimize health hazards and the threat to the environment (Ghaedi et al., 2013a; Mirzaei et al., 2013). However, dyes are relatively difficult to biodegrade and remove from dye wastewater due to their high solubility in water and complex aromatic molecular structures (Kayan et al., 2010; Yao et al., 2010). Providing an effective method

* *Corresponding author.*
E-mail: hyxia@kmust.edu.cn (Hongying Xia)

http://dx.doi.org/10.1016/j.jes.2016.12.027

to control and manage dye wastewater is thus of great urgency.

There are many dye wastewater treatment methods available including coagulation (Tunay et al., 1996), reverse osmosis (Forgacs et al., 2004), photo-degradation (Zhai et al., 2011), chemical oxidation (Tehrani-Bagha et al., 2010), membrane filtration methods (Alventosa-deLara et al., 2012), ozonation (Robinson et al., 2001), and biosorption (Ghaedi et al., 2013b). However, the abovementioned methods are generally ineffective in dye wastewater treatment or have high operating costs. Adsorption has attracted our attention owe to its many advantages such as high efficiency, environmental friendliness and low cost compared to other treatment methods for dye wastewater. Activated carbon, a material having an abundant porous structure and strong adsorption capacity, is widely used in many different industries, including in separation, removal of dyes and pollutants from wastewater, and as a catalyst support (Auta and Hameed, 2013; Ge et al., 2016). It is capable of adsorbing many kinds of dyes, but its adsorption efficiency and adsorption capacity is low. These disadvantages restrict its extensive application.

To overcome these disadvantages, more and more attention has been paid to the modification of activated carbons and synthesis of high performance adsorbents to treat dye wastewater. A popular method is using metal oxides to modify activated carbon. Modifying activated carbon with metal oxides may provide a structure with enhanced porosity, which can be varied in terms of pore structure and surface functional groups (Ge et al., 2016). Therefore, its adsorption properties are altered. According to literature reports, metal oxides such as aluminum oxide, iron oxide, zinc oxide, manganese oxide, copper oxide and vanadium oxide have been used to impregnate activated carbon to enhance its adsorption capability or improve its catalytic oxidation capability for dye wastewater (Chen et al., 2014; Fang et al., 2013; Yurum et al., 2014). Roosta et al. (2015) successfully synthesized a kind of modified carbon material ($Zn(OH)_2$-NP-AC), which has good performance in the removal of sunset yellow from aqueous solutions. Shah et al. (2014) also prepared a FeAC material *via* iron doping of activated carbon. The results show that FeAC is capable of up to 98% methylene blue (MB) removal from aqueous media. Goscianska et al. (2015) reported ordered mesoporous carbons modified with cerium as effective adsorbents for azo dye removal. Though many studies have been devoted to preparing and synthesizing various kinds of highly effective adsorbents, adsorbents based on single metal oxides have some disadvantages. Recently, composite adsorbents impregnated with two or more different metal oxides have attracted considerable research attention. The reason is that they could possess the advantages of multiple kinds of metal oxides as compared to adsorbents prepared with a single metal oxide (Su et al., 2015). What is more, they could show synergistic effects that greatly improve their adsorption performance (Ren et al., 2012).

Various rare earth compounds have been extensively developed as adsorbents for hazardous anions from aqueous solutions and have shown promising results (Deng and Yu, 2012; Liu et al., 2002). Iron oxides are also regarded as promising materials in dye wastewater treatment owing to Fe_3O_4 having magnetic properties (Xu et al., 2012; Gong et al., 2009). This means that adsorbents including Fe_3O_4 can be easily separated from dye wastewater in an external magnetic field. However, to the best of our knowledge, there have been a limited number of studies regarding synthesis of Fe–Ce composite modified activated carbon, based on the advantages of both types of oxides. In this work, we present a technical route whereby the raw activated carbon is treated with ultrasound and impregnated with $Fe(NO_3)_3$ and $Ce(NO_3)_3$, forming a kind of composite adsorbent (Fe–Ce-AC) by microwave heating. The cationic organic dye MB is a basic dye widely used in the abovementioned industrial applications. Therefore, MB was selected as the model pollutant to test the removal performance of the Fe–Ce-AC composite. In addition, we also thoroughly studied the equilibrium isotherm and kinetics of the adsorption process. Both the raw activated carbon and Fe–Ce-AC were characterized by using a number of characterization techniques.

1. Experimental

1.1. Materials and methods

The raw activated carbon was purchased from the Chengdu Kelong Chemical Reagent Factory of China. Chemical reagents including $Fe(NO_3)_3$ (China, Tianjin Reagent Chemicals Co., LTD), $Ce(NO_3)$ (China, Tianjin Reagent Chemicals Co., LTD) and MB (China, Tianjin Standard Technology Company) were all of analytical grade. The raw activated carbon was treated by ultrasound for 30 min (ultrasound-activated carbon) to clean off the impurities on the surface of the activated carbon by ultrasonic cavitation, to prepare for impregnation. Afterwards, 15 g of dry ultrasound-activated carbon was placed in 150 mL of an aqueous solution with $Fe(NO_3)_3$/$Ce(NO_3)$ mole ratio of 4/2 (using a mixture of 0.1 mol/L of $Fe(NO_3)_3$ and $Ce(NO_3)_3$ solution) for 3 hr. Then, the suspension was filtered and the solid was dried at 105°C for 24 hr. Finally, the sample was heated in a microwave furnace with microwave power of 700 W, temperature of 700°C and heating time of 25 min. The microwave furnace utilized multi-mode continuously controllable microwave power for the experiments. Table 1 lists the industrial analysis of the raw activated carbon and ultrasound-activated carbon. As shown in Table 1, the fixed carbon of the ultrasound-activated carbon is increased and other components are decreased because of ultrasonic cavitation, facilitating $Fe(NO_3)_3$ and $Ce(NO_3)_3$ impregnation.

1.2. Characterization methods

The N_2 adsorption measurement of Fe–Ce-AC was carried out at 77 K using an automatic adsorption apparatus (Autosorb-1-C, USA) with the relative pressure (P/P_0) range from 10^{-7} to 1. The total pore volumes were estimated as the equivalent liquid

Table 1 – Industry analysis on raw activated carbon and ultrasound-activated carbon.

	Ash (%)	Volatile (%)	Moisture (%)	Fixed carbon (%)
Raw activated carbon	3.29	3.99	1.9	92.72
Ultrasound-activated carbon	2.28	3.65	1.5	94.06

volume of the adsorbate (N_2) at a relative pressure of 0.99. The Brunauer–Emmett–Teller (BET) surface area of the samples was calculated by the BET equation. The pore size distribution was analyzed by using Non-Local Density Functional Theory (NLDFT). Zeta potential measurements were conducted using a ZetaPALS (Zeta Potential Analyzer using Phase Analysis Light Scattering, Brookhaven Instruments Corp., USA) with a voltage of 110–240 V and frequency of 50–60 Hz. Scanning electron microscopy (SEM, Philips XL30ESEM-TMP) analysis was used to assess the surface morphology. Fourier transform infrared spectroscopy (FTIR, Nicolet iS10, USA) was applied to qualitatively identify the chemical functional groups of the samples. Raman analysis was conducted for the samples using a Ramascope System 1000 (Renishaw, UK) with a laser excitation wavelength of 514.5 nm. Structural analysis was conducted with a powder X-ray diffractometer equipped with a Cu Ka X-ray source operating at 40 kV and 40 mA (D/max-3B, Rigaku, Japan). X-ray photoelectron spectroscopy (XPS) was performed on a PHI 5500 electron spectrometer (Physical Electronics, Inc., Chanhassen, MN, USA) using 200 W Mg radiation.

1.3. Adsorption experiments

The equilibrium isotherms of MB adsorption on raw activated carbon and Fe–Ce-AC were determined by batch adsorption tests in 150 mL Erlenmeyer flasks where 50 mL MB solutions with different initial concentrations (200–600 mg/L) at the pH of 6–7 were placed in the flasks. Weighing 0.1 g samples of raw activated carbon and Fe–Ce-AC with particle size of 71 μm were added to the flasks, which were kept in a thermostatted oscillator with shaking speed of 300 r/min at different temperatures (30, 40°C) until adsorption equilibrium was reached. After equilibrium was attained, the residual MB concentration was determined at 668 nm using a Ultraviolet–visible spectroscopy (UV–Vis) spectrophotometer. The amount of MB adsorbed onto the adsorbents, q_e (mg/g), was obtained under equilibrium conditions using the following equation:

$$q_e = (C_0 - C_e)V/M \quad (1)$$

where C_0 (mg/L) is the initial concentration of MB, and C_e (mg/L) is the equilibrium concentration of MB. V (L) and M (g) are the volume of the solution and weight of the adsorbents, respectively. Three commonly used isotherm equations, the Langmuir, Freundlich and Temkin isotherms, were applied to fit the adsorption data (Zhang et al., 2015). The parameters of these models are listed in Table 2.

Kinetic experiments were also carried out in 150 mL Erlenmeyer flasks, and the methods are almost the same as used in the isotherm studies. The flasks containing the MB and adsorbents were sampled at different time intervals. The amount of MB adsorbed at time t, q_t (mg/g), was calculated using the following equation:

$$q_t = (C_0 - C_t)V/M \quad (2)$$

where C_t (mg/L) is the liquid-phase concentration of MB solution at time t (min). In this study, three different models including the pseudo-first-order model, pseudo-second-order model and intraparticle diffusion model were applied to interpret the kinetic data (Gao et al., 2013). The parameters of the three models are listed in Table 3.

Table 2 – Adsorption isotherm models adopted in this work and their parameters.

Isotherm	Equation	Parameters
Langmuir isotherm	$\frac{1}{q_e} = \frac{1}{K_L Q_0 C_e} + \frac{1}{Q_0}$	C_e is the equilibrium concentration(mg/L) Q_0 (mg/g) is the adsorption constant related to adsorption capacity K_L (L/g) is the adsorption constant related to energy of adsorption
Freundlich isotherm	$\ln(q_e) = \ln(K_F) + \frac{1}{n}\ln(C_e)$	K_F is the adsorption constant related to adsorption capacity (mg/g). $(L/mg)^{1/n}$ n is the adsorption constant measuring the adsorption intensity
Temkin isotherm	$q_e = A + BLn(C_e)$	A and B are constants

2. Results and discussion

2.1. Characterization of pore structure

Fig. 1 shows the nitrogen adsorption isotherms (Fig. 1a), cumulative pore volumes (Fig. 1b) of ultrasound-activated carbon, raw activated carbon and Fe–Ce-AC and pore size distribution curve (Fig. 1c) of Fe–Ce-AC, respectively. These isotherms fall between types I and II, based on the International Union of Pure and Applied Chemistry (IUPAC) classification (Fig. 1a). All of them exhibit a high N_2 uptake at low relative pressures ($P/P_0 < 0.1$), indicating the presence of a large number of micropores. As Fig. 1a, b shows, the BET area and cumulative pore volume of the ultrasound-activated carbon is significantly increased compared to that of raw activated carbon owing to the fact that impurities on the raw activated carbon are removed *via* the "cavitation" of ultrasound. The BET area and cumulative pore volume of Fe–Ce-AC are less than those of the ultrasound-activated carbon, due to iron and cerium compounds occupying the pores, widening of pores in Fe–Ce-AC and some pores being destroyed after microwave heating. Pore size distribution is also a vital

Table 3 – Adsorption kinetic models adopted in this work and their parameters.

Kinetic models	Equation	Parameters
Pseudo-first order	$\ln(q_e - q_t) = \ln q_e - K_1 t$	q_e is the uptake of methylene blue at equilibrium (mg/g). K_1 (1/min) is the adsorption rate constant
Pseudo-second-order	$\frac{t}{q_e} = \frac{1}{K_2 q_e^2} + \frac{t}{q_e}$	K_2 (g/(mg·min)) is the rate constant of second-order equation
Intraparticle diffusion	$q_t = K_3\sqrt{t} + C$	K_3 mg/(g/$min^{1/2}$) is the intraparticle diffusion rate constant C is a constant

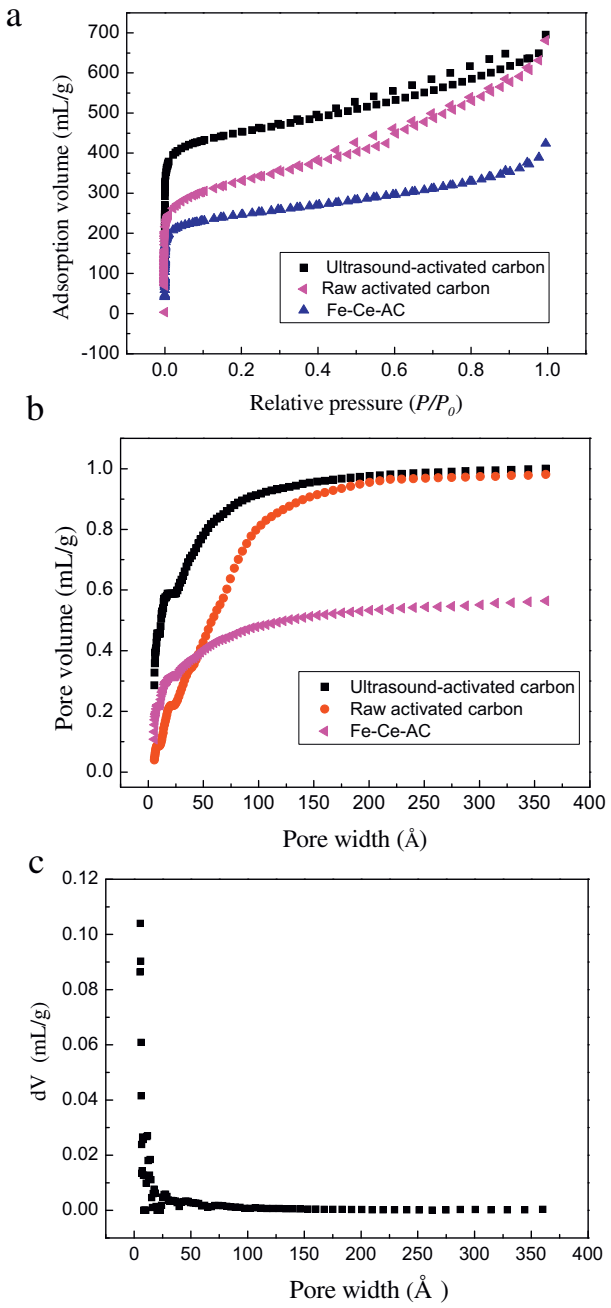

Fig. 1 – Nitrogen adsorption isotherm (a) and cumulative pore volume (b) of raw activated carbon, ultrasound-activated carbon and Fe–Ce-AC, pore distribution of Fe–Ce-AC (c).

indicator of adsorbents, which determines the fraction of the total pore volume accessible to molecules of a given size and shape. The average pore size of Fe–Ce-AC is 3.39 nm, which indicates that the Fe–Ce-AC is mesoporous due to most of the pores falling in the range from 1 to 4 nm (Fig. 1c). When the adsorbent pore diameter is at least 1.7 times larger than the size of the adsorbate, adsorption can occur (Cheng et al., 2016). Fe–Ce-AC (pore size 3.39 nm) can easily adsorb MB molecules given the MB molecular size of 0.8 nm.

Detailed comparisons of pore structure and MB removal values among activated carbons are shown in Table 4.

Table 4 – Details of pore structure and MB removal value of raw activated carbon, ultrasound-activated carbon and Fe–Ce-AC.

Subject	Raw activated carbon	Ultrasound-activated carbon	Fe–Ce-AC
BET surface area (m^2/g)	912	1257	776.2
Average pore diameter (nm)	5.51	3.07	3.39
Total pore volume (cm^3/g)	1.02	1.09	0.65
MB removal value(mg/g)	125	158	269

MB: methylene blue; BET: Brunauer–Emmett–Teller.

Compared with raw activated carbon, the average pore diameter of Fe–Ce-AC and ultrasound-activated carbon decreases. This indicates that the micropore proportion of these two kinds of activated carbons is larger, based on the difference in average pore size. The BET area and total pore volume of Fe–Ce-AC are less than that of ultrasound-activated carbon (Table 4), but the MB removal value of Fe–Ce-AC is larger. The result indicates that the iron oxides and cerium oxide coated onto the surface of the Fe–Ce-AC make a difference in MB removal.

2.2. Zeta potential measurement

Activated carbon-based adsorbents are usually considered amphoteric solids due to the presence of a variety of surface functional groups (Li et al., 2010). Therefore, the isoelectric point (IEP) of Fe–Ce-AC can be evaluated by determining the pH value at which the zeta potential is zero. IEP is used to qualitatively assess the polarity of the adsorbent surface charge (Song et al., 2010; Li et al., 2001). At pH < IEP, the adsorbent has positive surface charge and can act as an anion exchanger, while at pH > IEP, the surface charge of the adsorbent is negative, which is beneficial for adsorbing cations (Li et al., 2001). The IEP of Fe–Ce-AC is presented in Fig. 2. The IEP of Fe–Ce-AC is about 5.8 (Fig. 2). The pH value during the course of the adsorption experiment was about 6–7. Therefore, the Fe–Ce-AC had a negative surface charge and would adsorb MB by electrostatic attraction due to fact that MB is a cationic dye.

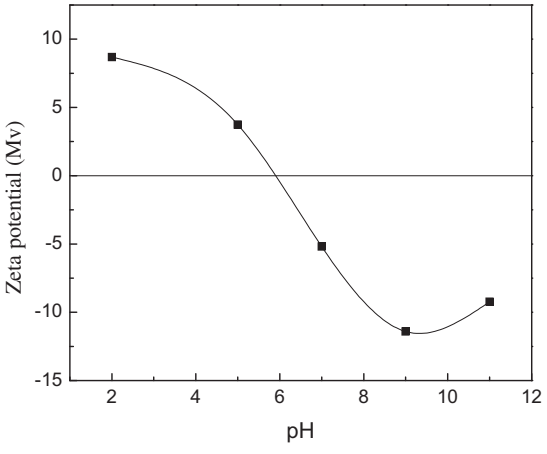

Fig. 2 – Zeta potential of Fe–Ce-AC samples at different pH.

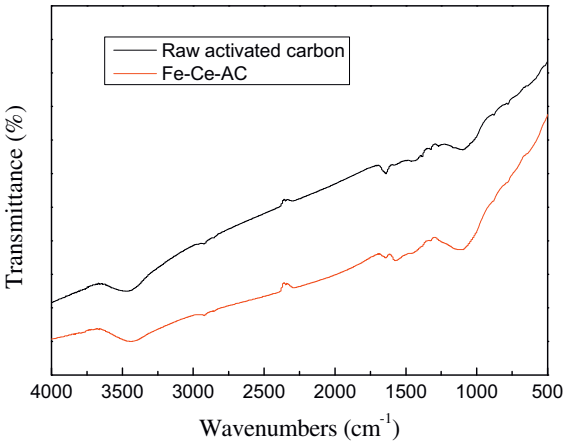

Fig. 3 – FTIR spectra of the raw activated carbon and Fe–Ce-AC. FTIR: Fourier transform infrared spectroscopy.

2.3. *FTIR analysis*

Fig. 3 shows the Fourier transform infrared spectra of raw activated carbon and Fe–Ce-AC. Some information about the chemical function groups of raw activated carbon and Fe–Ce-AC can be obtained from Fig. 3. As Fig. 3 shows, there is a small difference in the general shape of the spectra. The spectrum of raw activated carbon and Fe–Ce-AC has four obvious peaks at 3470, 1642, 1290 and 1098 cm^{-1}. The band at around 3470 cm^{-1} can be assigned to the O–H stretching vibration mode of hydroxyl functional groups, and the band at 1642 cm^{-1} can be assigned to C═C symmetrical stretching of pyrone and C═O of carboxylic groups (Ji et al., 2007; Moniruzzaman and Ono, 2013). The peak at 1290 and 1098 cm^{-1} can be assigned to –C–O (ester, ether and phenol) and C–O functional groups (Foo and Hameed, 2012).

2.4. *Raman analysis*

The Raman spectrum is applied in obtaining information about the molecular vibration or rotational energy of a sample, reflecting the degree of structural disorder. In particular, Raman spectroscopy is widely used to characterize the structural features of carbonaceous materials (Sadezky et al., 2005; Xu et al., 2015). The Raman spectra for raw activated carbon and Fe–Ce-AC are shown in Fig. 4. All the samples have two pronounced D and G bands, which are assigned to the disorder and defect level of the crystalline structure and graphitic structure of carbon materials, respectively (Nemanich and Solin, 1979; Zhou et al., 2015). As shown in Fig. 4, two prominent peaks appear at approximately 1340 (D band) and 1600 cm^{-1} (G band), which is the typical spectrum observed for carbon materials. The value of R (I_D/I_G) is defined to characterize the degree of disorder for carbon materials (Yao et al., 2016). I_D and I_G are calculated from the integrated intensity of the D and G peaks of the Raman spectrum, respectively (Yao et al., 2016). The I_D/I_G value of Fe–Ce-AC is larger than that of the raw activated carbon, indicating that the preparation process for Fe–Ce-AC slightly degraded the structure of the graphite crystallites. This also means that the degree of graphitization of Fe–Ce-AC decreased due to iron oxide and cerium oxide occupying the pore channels.

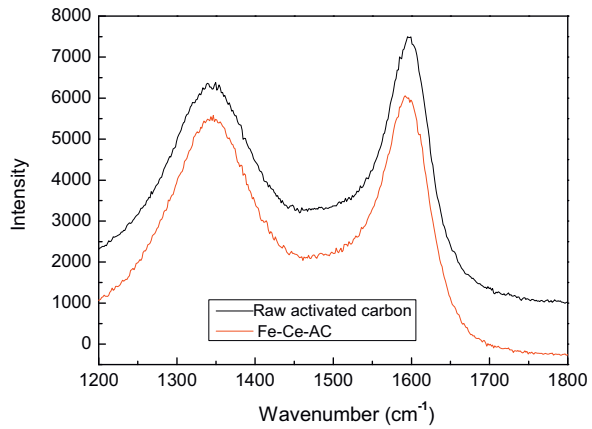

Fig. 4 – Raman spectrum for raw activated carbon and Fe–Ce-AC.

2.5. *X-ray diffraction (XRD) analysis*

Fig. 5 shows the XRD patterns of raw activated carbon and Fe–Ce-AC. As shown in Fig. 5a, the main component of raw activated carbon is carbon, having three major peaks with a

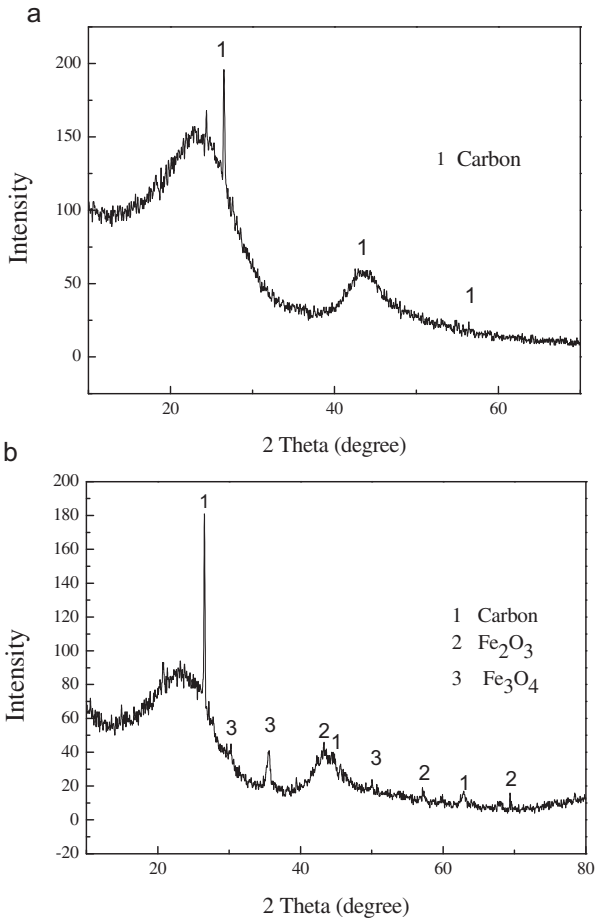

Fig. 5 – X-ray diffraction (XRD) spectra of the ultrasound-activated carbon (a) and Fe–Ce-AC (b).

number of impurity peaks. Compared with Fig. 5a, Fe–Ce-AC has a relatively smooth diffraction peak without many impurity diffraction peaks. As shown in Fig. 5b, Fe–Ce-AC shows peaks for three substances (C, Fe_2O_3 and Fe_3O_4). It was determined that $Fe(NO_3)_3$ was successfully impregnated onto the activated carbon and subsequently decomposed to form iron oxides. The presence of Fe_3O_4 leads to Fe–Ce-AC having magnetic properties. Hence, Fe–Ce-AC can be easily separated from dye wastewater at adsorption saturation under a magnetic field and facilitate adsorbent reuse. However, there were no observable peaks due to cerium oxides owing to the low cerium oxide contents. Comparing Fig. 5a and b, the peak intensity of Fe–Ce-AC is weak, indicating that the crystal structure of Fe–Ce-AC is not very ordered because part of the iron oxides and cerium oxide occupy pores. The results are consistent with the Raman analysis.

2.6. XPS analyses

To further illuminate the composition and surface groups of Fe–Ce-AC, the XPS technique was employed. As Fig. 6a shown, the wide scan XPS spectrum of Fe–Ce-AC indicates the presence of Ce, Fe, O and C. Fig. 6b shows the high-resolution Fe 2p scan of Fe–Ce-AC. As shown in Fig. 6b, the peaks at 710.7 and 725.2 eV correspond to the binding energies of Fe 2p3/2 and Fe 2p1/2, respectively. The reported values for Fe^{2+} 2p3/2 and Fe^{3+}2p3/2 are 709 and 711 eV, respectively (Tong et al., 2011); in this work, the peaks at binding energy of around 710.7 eV in Fe–Ce-AC correspond to Fe 2p 3/2 photoelectron peaks of iron oxides (Chen et al., 2011; Xi et al., 2014), confirming that both ferrous oxides and ferric oxides are present. Fig. 6c presents the analysis of the Ce 3d core level spectra, confirming that cerium is present. Details of the analysis procedure are given elsewhere. Fig. 6d shows the photoelectron peak from O 1s, which is resolved into four peaks. The deconvolution of the O 1s signal indicated the presence of CeO_2 and Ce_2O_3 at binding energies of 529.6 and 530.2, respectively (Niroumandrad et al., 2015; Song et al., 2012). The peak at about 530.7 eV is assigned to the oxygen in Fe–O of Fe–Ce-AC, indicating that iron oxides are present. The peak at 532.2 eV arises from hydroxyl groups on the surface, oxygen chemisorbed on the surface in other forms such as CO, CO_2, or grain boundary impurities (Kotani and Ogasawara, 1992; Murugan et al., 2015). The result is in good agreement with the XRD analysis.

2.7. Microscopic structure analysis

Fig. 7(a–c) shows the SEM images of raw activated carbon, ultrasound-activated carbon and Fe–Ce-AC, respectively. As shown in Fig. 7a, the pore structure of raw activated carbon is not clearly visible, and the surface is covered by a large amount of impurities. As Fig. 7b shows, the surface of ultrasound-activated carbon is clean and the pore structure is easy to see as a result of the ultrasound treatment. Fig. 7c shows a clear pore structure. However, the surface of Fe–Ce-AC has a number of gray deposits, which may be iron oxides and cerium oxides. Fig. 7d–e shows the Energy dispersive X-ray Spectroscopy (EDX) of Fe–Ce-AC. The EDX result shows that the Fe–Ce-AC has some content of Fe and Ce compounds. The results are in good agreement with XRD and XPS. The stability of the iron oxides

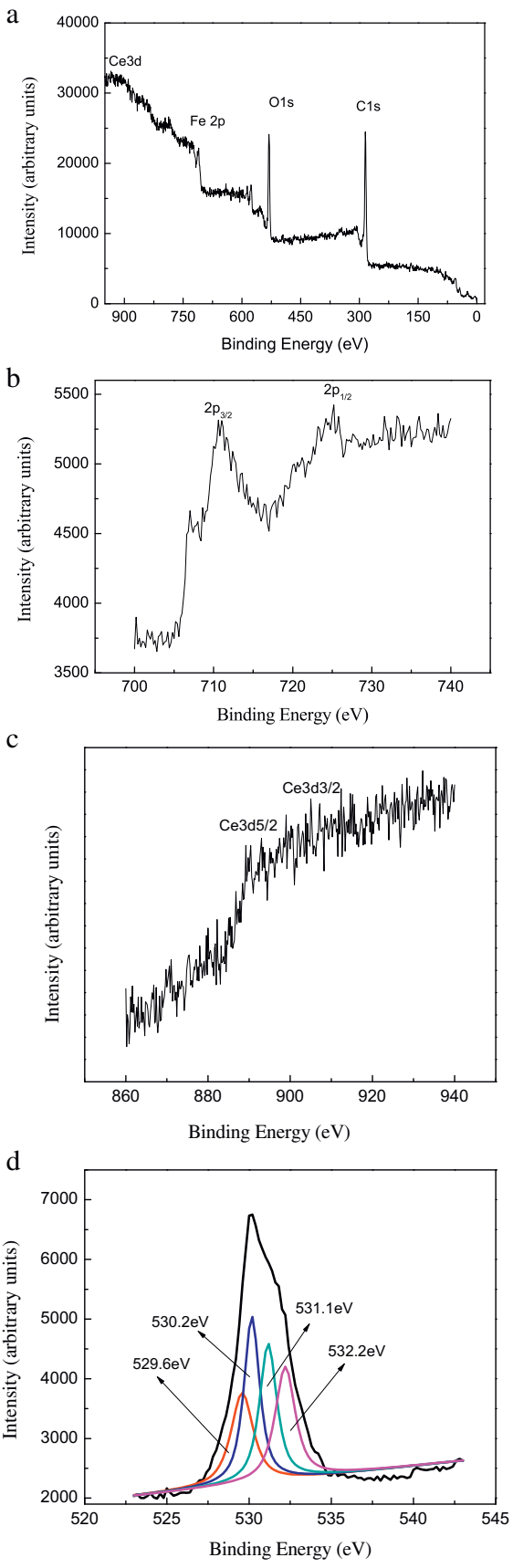

Fig. 6 – The wide scan XPS spectrum (a), the peaks Fe 2p (b), the peaks Ce 3d (c), the peaks O 1s of Fe–Ce-AC (d). XPS: X-ray photoelectron spectroscopy.

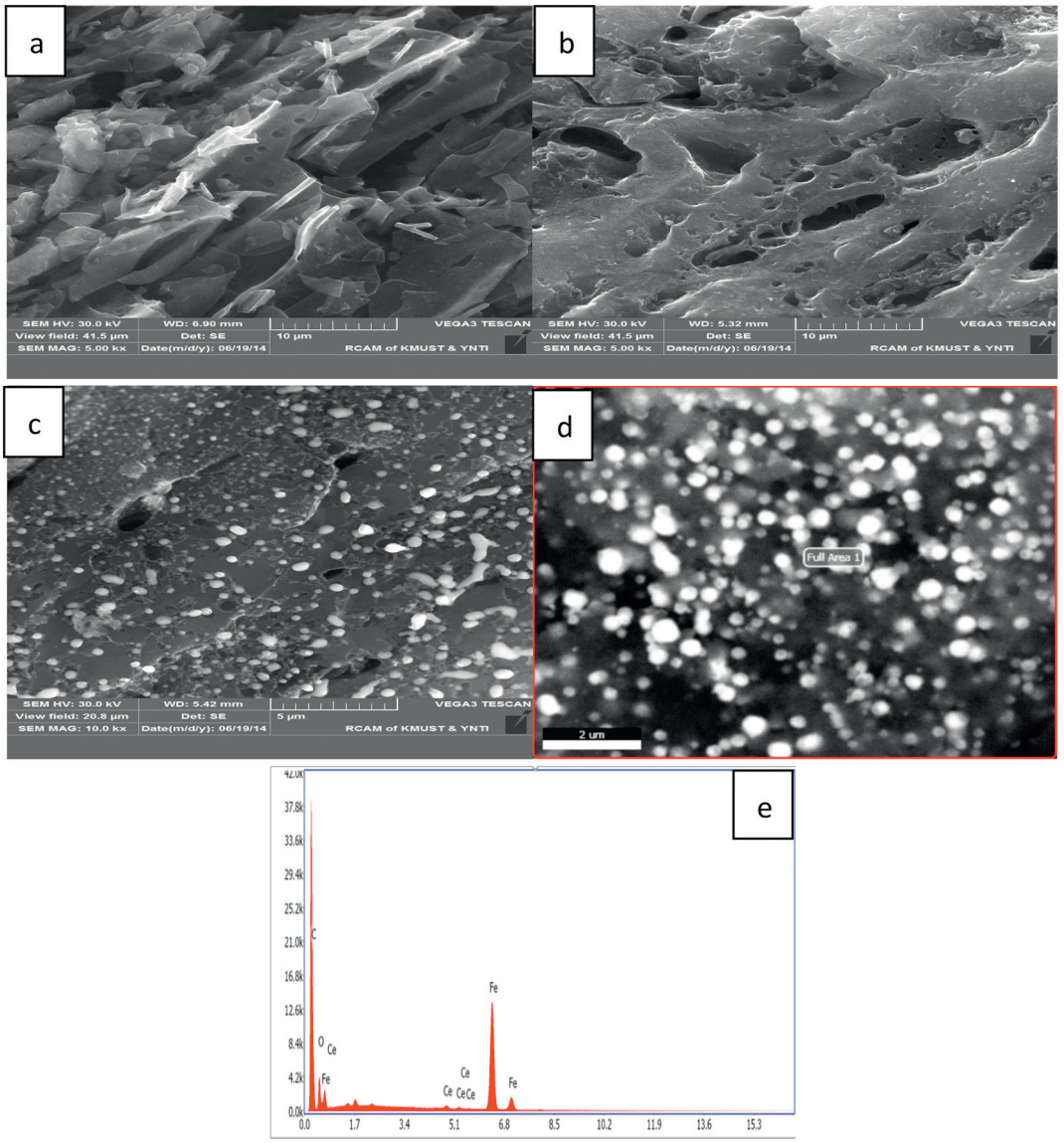

Fig. 7 – SEM images of the raw activated carbon (a), ultrasound-activated carbon (b), Fe–Ce-AC (c) and Energy dispersive X-ray Spectroscopy (EDX) Fe–Ce-AC (d–e). SEM: scanning electron microscopy.

and cerium oxides was also tested in leaching experiments. The amount of Fe and Ce leached was very slight (both <5 mg/L). The results show that the stability of iron oxides and cerium oxides coated onto Fe–Ce-AC is very good.

2.8. Adsorption isotherm studies

Adsorption isotherms were studied to analyze the adsorption mechanisms and evaluate how adsorbate molecules on the

Table 5 – Adsorption isotherm parameters for adsorption of raw activated carbon and Fe–Ce-AC at different temperatures.

	Tem (°C)	Langmuir			Freundlich			Temkin
		K_L (L/mg)	Q_m (mg/g)	R^2	1/*n*	lnK_F	R^2	R^2
Raw activated carbon	30	0.477	178.25	0.999	0.194	4.718	0.879	0.954
	40	0.685	192.31	0.999	0.191	4.683	0.893	0.959
	Tem (°C)	Langmuir			Freundlich			Temkin
		K_L (L/mg)	Q_m (mg/g)	R^2	1/*n*	lnK_F	R^2	R^2
Fe–Ce-AC	30	0.349	255.76	0.995	0.194	4.732	0.874	0.960
	40	0.391	264.55	0.996	0.187	4.710	0.873	0.953

adsorbent are distributed. In this work, three isotherm models were used to determine which one is the best match for the adsorption process, and the fitting results of the three isotherm models are presented in Table 5. As Table 5 shows, the R^2 value of the Langmuir isotherm was larger than that of the other two, indicating that the Langmuir isotherm was the best fit to the experimental data. The Freundlich and Temkin isotherms, however, did not match the experimental data well. Moreover, another characteristic parameter of the Langmuir isotherm that can be used to evaluate the feasibility of adsorption on an adsorbent is the dimensionless factor R_L, called the separation factor. It can be calculated by the following equation:

$$R_L = \frac{1}{1 + K_L C_0} \quad (3)$$

where C_0 corresponds to the initial concentration of MB and K_L is the Langmuir constant. The value of R_L is related to the type of isotherm: unfavorable ($R_L > 1$), linear ($R_L = 1$), favorable ($0 < R_L < 1$), and irreversible ($R_L = 0$) (Guo et al., 2009). The R_L values for MB adsorption onto the adsorbents were calculated to be in the range of 0.0024–0.0105 for raw activated carbon, and 0.0024–0.0104 for Fe–Ce-AC. Hence, the Langmuir isotherm is the most appropriate match for the experimental data for the adsorbents. The findings also show that MB tends to exhibit monolayer adsorption on activated carbon. Compared with raw activated carbon, the maximum monolayer adsorption capacity of Fe–Ce-AC increased by 27.31%, indicating that the preparation methods for Fe–Ce-AC are feasible and Fe–Ce-AC can be used as an effective adsorbent for MB removal. It is well known that an increase in temperature could accelerate the rate of diffusion of the adsorbate molecules across the external boundary layer and in the internal pores of the adsorbent particle due to the decrease in the viscosity of the solution. The amount of MB adsorbed on Fe–Ce-AC increased from 255.76 to 264.55 mg/g with the increase of solution temperature from 303 to 313 K. Theydan and Ahmed reported similar results (Theydan and Ahmed, 2012). The explanation for this result is that the surface activity and kinetic energy gradually increased with increasing temperature, which will lead to the interaction forces between the solute and adsorbent becoming stronger than those between solute and solvent (Theydan and Ahmed, 2012). The MB adsorption onto the raw activated carbon and Fe–Ce-AC for the Langmuir isotherm at different temperatures is shown in Fig. 8. Fig. 9 shows a photograph of an MB solution treated using Fe–Ce-AC (b) and untreated MB solution (a). As Fig. 9 shows, the MB dye almost completely disappeared due to the remarkable treatment *via* Fe–Ce-AC. The result shows that Fe–Ce-AC can be used as an effective adsorbent to adsorb MB. What's more, the Fe–Ce-AC in the MB solution is attracted by a magnet. The phenomenon proves that Fe–Ce-AC is magnetic. The result is in good agreement with the XRD analysis.

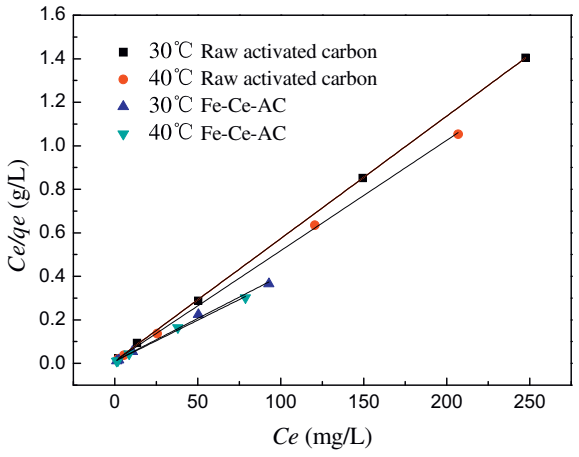

Fig. 8 – Langmuir isotherms for MB adsorption onto raw activated carbon and Fe–Ce-AC at different temperatures. MB: methylene blue.

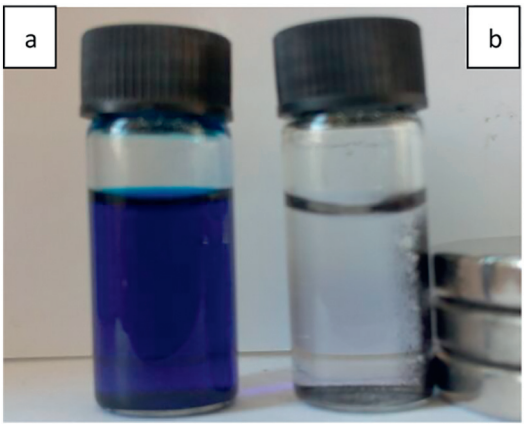

Fig. 9 – Photographs of MB solutions (a) and treated using Fe–Ce-AC (b). MB: methylene blue.

The maximum monolayer adsorption capacity of various adsorbents for MB is listed in Table 6 (Gao et al., 2012; Gercel et al., 2007; Haque et al., 2011; Mahapatra et al., 2012; Song et al., 2015; Zhang et al., 2014). The Q_0 of Fe–Ce-AC is the largest compared to those reported, suggesting that Fe–Ce-AC has great potential application in MB removal.

2.9. Adsorption kinetics studies

Adsorption kinetics studies can provide important parameters for the adsorption process. In order to study the mechanism of MB adsorption, pseudo-first-order and pseudo-second-order

Table 6 – Maximum monolayer adsorption capacity of various adsorbents for MB.

Adsorbents	Maximum monolayer adsorption capacity (mg/g)	References
Fe–Ce-AC	264.55	This study
Raw activated carbon	192.31	This study
MCNCs-050	52.91	Gao et al. (2012)
ZnS:Cu-NP-AC	123.46	Gercel et al. (2007)
Euphorbia rigida-carbon	114.45	Haque et al. (2011)
Fe3O4@GPTMS@Lys	185	Mahapatra et al. (2012)
Ag-NP-AC	71.43	Song et al. (2015)
CuO-NP-AC	10.55	Zhang et al. (2014)

MB: methylene blue.

Table 7 – Kinetic and intraparticle diffusion parameters for adsorption of raw activated carbon and Fe–Ce-AC at different temperatures.

T (°C)	Pseudo-first-order			Pseudo-first-order		
	K_1 (1/min)	R^2	Q_e	K_1 (1/min)	R^2	Q_e
30	0.00133	0.977	112.285	0.00341	0.979	62.479
40	0.00221	0.956	71.516	0.01919	0.901	30.444
T (°C)	Pseudo-second-order			Pseudo-second-order		
	Q_e (mg/g)	R^2	K_2 (g/(mg·min))	Q_e (mg/g)	R^2	K_2 (g/(mg·min))
30	208.333	0.999	0.000623	204.499	0.999	0.000941
40	165.290	0.998	0.000747	168.350	0.998	0.000745
T (°C)	Intraparticle diffusion model			Intraparticle diffusion model		
	C (mg/g)	K_3 (mg/g $min^{1/2}$)	R^2	C (mg/g)	K_3 (mg/g $min^{1/2}$)	R^2
30	152.885	3.719	0.955	165.17	2.679	0.917
40	125.006	2.569	0.977	128.237	2.547	0.978

models were applied to examine the adsorption process, while the diffusion mechanism was examined with the intraparticle diffusion model. The model parameters calculated for the three of models are listed in Table 7. The goodness of fit between the experimental values and the model calculated results was evaluated by the R^2 values (correlation coefficients). A higher R^2 value indicates that a model can be considered more applicable to describe MB adsorption onto the adsorbent. As shown in Table 7, the pseudo-second-order kinetic model has the highest R^2 value among three models both for raw activated carbon and Fe–Ce-AC. In other words, the pseudo-second-order model can be applied to describe the adsorption process. According to Table 7, we found that the adsorption rate K_2 of the pseudo-second-order model decreases with increasing temperature. The phenomenon shows that the adsorption process more easily occurs at low temperature. On the whole, the K_2 for Fe–Ce-AC is larger than that of raw activated carbon. This proves that Fe–Ce-AC has a larger adsorption rate, indicating that Fe–Ce-AC has good performance. Fig. 10 shows the pseudo-second-order model for adsorption of MB onto raw activated carbon and Fe–Ce-AC at 400 ml/L at different temperatures.

The intraparticle diffusion model given by Weber and Morris is also typically employed to further investigate the rate-controlling step of the adsorption process (Jagtap et al., 2011). The rate-controlling step of adsorption onto Fe–Ce-AC mainly depends on either surface or pore diffusion (Foo and Hameed, 2011). The R^2 values (Table 7) for this model were lower compared to those obtained from pseudo-second-order models. For the plot of q_t *versus* $t_{1/2}$ (Fig. 11), the first steeper portion is the instantaneous adsorption or external surface adsorption. The second portion is the gradual adsorption stage, where intraparticle diffusion is the rate-limiting process. In some cases, a third portion exists, which is the final equilibrium stage where intraparticle diffusion starts to slow down due to extremely low adsorbate concentrations left in the solution. As shown in Fig. 11, the plot did not pass through the origin, and this deviation from the origin or near saturation might be due to the difference in mass transfer rate in the initial and final stages of adsorption. From these results, it can be concluded that intraparticle diffusion is not the dominant mechanism for the adsorption of MB from aqueous solution by Fe–Ce-AC. In other words, the results also prove that intraparticle diffusion is not the rate-limiting step in the MB adsorption process.

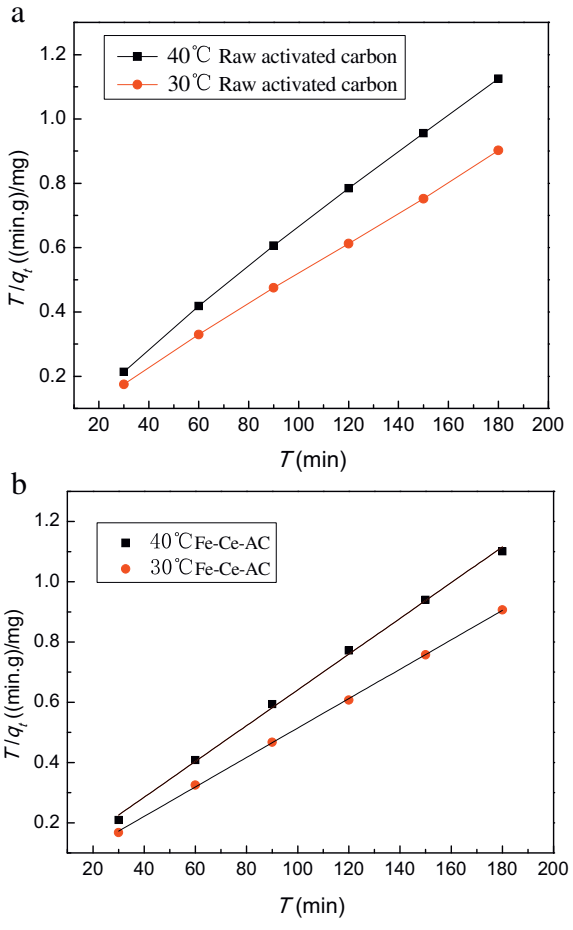

Fig. 10 – Pseudo-second-order kinetics for adsorption of MB onto raw activated carbon (a) and Fe–Ce-AC (b) at different temperatures. MB: methylene blue.

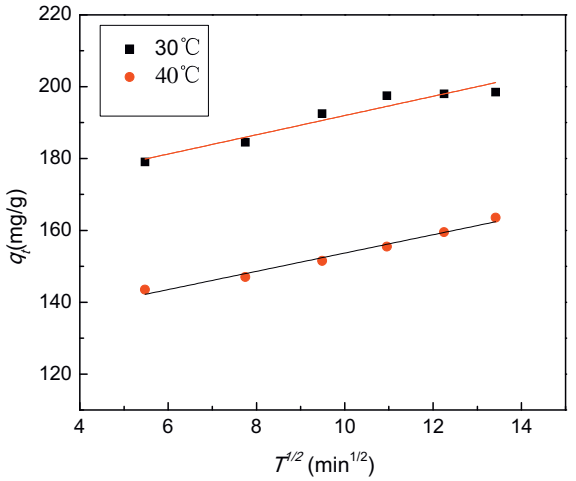

Fig. 11 – Intraparticle diffusion model for the adsorption of MB onto Fe–Ce-AC at t 30°C and 40°C. Adsorbent 0.1 g; 50 mL MB solution; MB concentration 400 mg/L. MB: methylene blue.

3. Conclusions

Fe–Ce-AC was prepared by microwave heating after ultrasonic pretreatment, and exhibited good MB removal capacity. In this work, the physico-chemical properties of Fe–Ce-AC were characterized by N_2 adsorption, zeta potential measurement, FTIR, Raman, XPS, XRD SEM and Energy dispersive X-ray Spectroscopy (EDS). The surface chemistry and textural properties of Fe–Ce-AC changed when it was modified by iron/cerium *via* microwave heating. The MB removal efficiency is significant. Compared with raw activated carbon, the maximum monolayer adsorption capacity of Fe–Ce-AC increased by 27.31%. In addition, adsorption isotherms and adsorption kinetics were thoroughly studied for the dye wastewater treatment. The equilibrium data fit well with the Langmuir model. The kinetic data tended to match well with the pseudo-second-order model. The above analyses proved the successful application of Fe–Ce-AC for effective removal of MB, providing a new promising adsorbent for dye wastewater.

Acknowledgments

The authors would like to express their gratitude to the Specialized Research Fund for the National Natural Science Foundation of China (Nos.21567013, 51504119), the National High Technology Research and Development Program (863) of China (No. 2015AA020201, the Yunnan Applied Basic Research Project (No.2015FB129), and the Yunnan Provincial Science and Technology Innovation Talents Scheme Technological Leading Talent (No.2013HA002).

REFERENCES

Alventosa-deLara, E., Barredo-Damas, S., Alcaina-Miranda, M.I., Iborra-Clar, M.I., 2012. Ultrafiltration technology with a ceramic membrane for reactive dye removal: optimization of membrane performance. J. Hazard. Mater. 209, 492–500.

Auta, M., Hameed, B.H., 2013. Acid modified local clay beads as effective low-cost adsorbent for dynamic adsorption of methylene blue. J. Ind. Eng. Chem. 19, 1153–1161.

Chen, H., Luo, H.J., Lan, Y.C., Dong, T.T., Hu, B.J., Wang, Y.P., 2011. Removal of tetracycline from aqueous solutions using polyvinylpyrrolidone (PVP-K30) modified nanoscale zero valent iron. J. Hazard. Mater. 192, 44–53.

Chen, C.M., Wei, L.Y., Guo, X., Guo, S.H., Yan, G.X., 2014. Investigation of heavy oil refinery wastewater treatment by integrated ozone and activated carbon-supported manganese oxides. Fuel Process. Technol. 124, 165–173.

Cheng, S., Zhang, L., Xia, H., Peng, J., Shua, J., Li, C., 2016. Ultrasound and microwave-assisted preparation of Fe-activated carbon as an effective low-cost adsorbent for dyes wastewater treatment. RSC Adv. 6, 78936–78946.

Deng, H., Yu, X.L., 2012. Adsorption of fluoride, arsenate and phosphate in aqueous solution by cerium impregnated fibrous protein. Chem. Eng. J. 184, 205–212.

Fang, H.B., Zhao, J.T., Fang, Y.T., Huang, J.J., Wang, Y., 2013. Selective oxidation of hydrogen sulfide to sulfur over activated carbon-supported metal oxides. Fuel 108, 143–148.

Foo, K.Y., Hameed, B.H., 2011. Microwave assisted preparation of activated carbon from pomelo skin for the removal of anionic and cationic dyes. Chem. Eng. J. 173, 385–390.

Foo, K.Y., Hameed, B.H., 2012. Factors affecting the carbon yield and adsorption capability of the mangosteen peel activated carbon prepared by microwave assisted K_2CO_3 activation. Chem. Eng. J. 180, 66–74.

Forgacs, E., Cserhati, T., Oros, G., 2004. Removal of synthetic dyes from wastewaters: a review. Environ. Int. 30, 953–971.

Gao, P., Liu, Z.H., Xue, G., Han, B., Zhou, M.h., 2012. Preparation and characterization of activated carbon produced from rice straw by $(NH_4)_2HPO_4$ activation. Bioresour. Technol. 102, 3645–3648.

Gao, H.J., Zhao, S.Y., Cheng, X.Y., Wang, X.D., Zheng, L.Q., 2013. Removal of anionic azo dyes from aqueous solution using magnetic polymer multi-wall carbon nanotube nanocomposite as adsorbent. Chem. Eng. J. 223 (5), 84–90.

Ge, X.Y., Wu, Z.S., Wu, Z.L., Yan, Y.J., Cravotto, G., Ye, B.C., 2016. Enhanced PAHs adsorption using iron-modified coal-based activated carbon via microwave radiation. J. Taiwan Inst. Chem. Eng. 64, 235–243.

Gercel, O., Ozcan, A., Ozcan, A.S., Gercel, H.F., 2007. Preparation of activated carbon from a renewable bio-plant of *Euphorbia rigida* by H2SO4 activation and its adsorption behavior in aqueous solutions. Appl. Surf. Sci. 253, 4843–4852.

Ghaedi, M., Ghayedi, M., Kokhdan, S.N., Sahraei, R., Daneshfar, A., 2013a. Palladium, silver, and zinc oxide nanoparticles loaded on activated carbon as adsorbent for removal of bromophenol red from aqueous solution. J. Ind. Eng. Chem. 19, 1209–1217.

Ghaedi, M., Hajati, S., Barazesh, B., Karimi, F., Ghezelbash, G., 2013b. *Saccharomyces cerevisiae* for the biosorption of basic dyes from binary component systems and the high order derivative spectrophotometric method for simultaneous analysis of Brilliant green and Methylene blue. J. Ind. Eng. Chem. 19, 227–233.

Ghaedi, M., Nasab, A.G., Khodadoust, S., Sahraei, R., Daneshfar, A., 2015. Characterization of zinc oxide nanorods loaded on activated carbon as cheap and efficient adsorbent for removal of methylene blue. J. Ind. Eng. Chem. 21 (21), 986–993.

Gong, J.L., Wang, B., Zeng, G.M., Yang, C.P., Niu, C.G., Niu, Q.Y., et al., 2009. Removal of cationic dyes from aqueous solution using magnetic multi-wall carbon nanotube nanocomposite as adsorbent. J. Hazard. Mater. 164 (2–3), 1517–1522.

Goscianska, J., Marciniak, M., Pietrzak, R., 2015. Ordered mesoporous carbons modified with cerium as effective adsorbents for azo dyes removal. Sep. Purif. Technol. 154, 236–245.

Guo, S.H., Li, W., Zhang, L.B., Peng, J.H., Xia, H.Y., Zhang, S.M., 2009. Kinetics and equilibrium adsorption study of lead(II) onto the low cost adsorbent-*Eupatorium adenophorum* spreng. Process. Saf. Environ. 87, 343–351.

Haque, E., Jun, J.W., Jhung, S.H., 2011. Adsorptive removal of methyl orange and methylene blue from aqueous solution with a metal-organic framework material, iron terephthalate (MOF-235). J. Hazard. Mater. 185, 507–511.
Jagtap, S., Yenkie, M.K., Das, S., Rayalu, S., 2011. Synthesis and characterization of lanthanum impregnated chitosan flakes for fluoride removal in water. Desalination 273, 267–275.
Ji, Y.B., Li, T.H., Zhu, L., Wang, X.X., Lin, Q., 2007. Preparation of activated carbons by microwave heating KOH activation. Appl. Surf. Sci. 254, 506–512.
Kayan, B., Gozmen, B., Demirel, M., Gizir, A.M., 2010. Degradation of acid red 97 dye in aqueous medium using wet oxidation and electro-Fenton techniques. J. Hazard. Mater. 177, 95–102.
Kotani, A., Ogasawara, H., 1992. Theory of core-level spectroscopy of rare-earth oxides. J. Electron Spectrosc. 60, 257–299.
Li, Y.H., Wang, S., Cao, A., Zhao, D., Zhang, X., Xu, C., et al., 2001. Adsorption of fluoride from water by amorphous alumina supported on carbon nanotubes. Chem. Phys. Lett. 350, 412–416.
Li, Y.H., Du, Q.J., Wang, X.D., Zhang, P., Wang, D.H., Wang, Z.H., et al., 2010. Removal of lead from aqueous solution by activated carbon prepared from *Enteromorpha prolifera* by zinc chloride activation. J. Hazard. Mater. 18, 583–589.
Liu, R.X., Guo, J.L., Tang, H.X., 2002. Adsorption of fluoride, phosphate, and arsenate ions on a new type of ion exchange fiber. J. Colloid Interface Sci. 248, 268–274.
Mahapatra, K., Ramteke, D.S., Paliwal, L.J., 2012. Production of activated carbon from sludge of food processing industry under controlled pyrolysis and its application for methylene blue removal. J. Anal. Appl. Pyrolysis 95, 79–86.
Mirzaei, A., Ebadi, A., Khajavi, P., 2013. Kinetic and equilibrium modeling of single and binary adsorption of methyl tert-butyl ether (MTBE) and tert-butyl alcohol (TBA) onto nano-perfluorooctyl alumina. Chem. Eng. J. 231, 550–560.
Moniruzzaman, M., Ono, T., 2013. Separation and characterization of cellulose fibers from cypress wood treated with ionic liquid prior to laccase treatment. Bioresour. Technol. 127, 132–137.
Murugan, R., Vijayaprasath, G., Ravi, G., 2015. The influence of substrate temperature on the optical and micro structural properties of cerium oxide thin films deposited by RF sputtering. Superlattice. Microst. 85, 321–330.
Nemanich, R.J., Solin, S.A., 1979. First-and second-order Raman scattering from finite-size crystals of graphite. Phys. Rev. B 20, 392–401.
Nethaji, S., Sivasamy, A., 2011. Adsorptive removal of an acid dye by lignocellulosic waste biomass activated carbon: equilibrium and kinetic studies. Chemosphere 82, 1367–1372.
Niroumandrad, S., Rostami, M., Ramezanzadeh, B., 2015. Corrosion resistance of flaky aluminum pigment coated with ceriumoxides/hydroxides in chloride and acidic electrolytes. Appl. Surf. Sci. 357, 2121–2130.
Ren, Z.M., Shao, L.N., Zhang, G.S., 2012. Adsorption of phosphate from aqueous solution using an iron–zirconium binary oxide sorbent. Water Air Soil Pollut. 223, 4221–4231.
Robinson, T., McMullan, G., Marchant, R., Nigam, P., 2001. Remediation of dyes in textile effluent: a critical review on current treatment technologies with a proposed alternative. Bioresour. Technol. 77, 247–255.
Roosta, M., Ghaedi, M., Sahraei, R., Purkait, M.K., 2015. Ultrasonic assisted removal of sunset yellow from aqueous solution by zinc hydroxide nanoparticle loaded activated carbon: optimized experimental design. Mater. Sci. Eng. C Mater. 52, 82–89.
Rosenkranz, H.S., Cunningham, S.L., Mermelstein, R., Cunningham, A.R., 2007. The challenge of testing chemicals for potential carcinogenicity using multiple short-term assays: an analysis of a proposed test battery for hair dyes. Mutat. Res. Genet. Toxicol. Environ. 633, 55–66.
Sadezky, A., Muckenhuber, H., Grothe, H., Niessner, R., Pöschl, U., 2005. Raman microspectroscopy of soot and related carbonaceous materials: spectral analysis and structural information. Carbon 43, 1731–1742.
Shah, I., Adnan, R., Ngah, W.S.W., Mohamed, N., Taufiq-Yap, Y.H., 2014. A new insight to the physical interpretation of activated carbon and iron doped carbon material: sorption affinity towards organic dye. Bioresour. Technol. 160, 52–56.
Song, X., Liu, H., Cheng, L., Qu, Y., 2010. Surface modification of coconut-based activated carbon by liquid-phase oxidation and its effects on lead ion adsorption. Desalination 255, 78–83.
Song, D., Feng, X.G., Sun, M.R., Ma, X.X., Tang, G.Z., 2012. Composition and corrosion resistance of cerium conversion films on 2195Al–Li alloy. J. Rare Earths 3, 383–387.
Song, Y.B., Lv, S.N., Cheng, C.J., Ni, G.L., Xie, X.W., Huang, W., et al., 2015. Fast and highly-efficient removal of methylene blue from aqueous solution by poly (styrenesulfonic acid-co-maleic acid)-sodium-modified magnetic colloidal nanocrystal clusters. Appl. Surf. Sci. 324, 854–863.
Su, Y., Yang, W.Y., Sun, W.Z., Li, Q., Shang, J.K., 2015. Synthesis of mesoporous cerium–zirconium binary oxide nanoadsorbents by a solvothermal process and their effective adsorption of phosphate from water. Chem. Eng. J. 268, 270–279.
Tehrani-Bagha, A.R., Mahmoodi, N.M., Menger, F.M., 2010. Degradation of a persistent organic dye from colored textile wastewater by ozonation. Desalination 260, 34–38.
Theydan, S.K., Ahmed, M.J., 2012. Adsorption of methylene blue onto biomass-based activated carbon by $FeCl_3$ activation: equilibrium, kinetics, and thermodynamic studies. J. Anal. Appl. Pyrolysis 97, 116–122.
Tong, M., Yuan, S.H., Long, H.Y., Zheng, M.M., Wang, L.L., Chen, J., 2011. Reduction of nitrobenzene in groundwater by iron nanoparticles immobilized in PEG/nylon membrane. J. Contam. Hydrol. 122, 16–25.
Tunay, O., Kabdasli, I., Eremektar, G., Orhon, D., 1996. Color removal from textile wastewaters. Water Sci. Technol. 34 (34), 9–16.
Xi, Y.F., Sun, Z.M., Hreid, T., Ayoko, G.A., Frost, R.L., 2014. Bisphenol A degradation enhanced by air bubbles via advanced oxidation using in situ generated ferrous ions from nano zero-valent iron/palygorskite composite materials. Chem. Eng. J. 24, 66–74.
Xu, P., Zeng, G.M., Huang, D.L., Feng, C.L., Hu, S., Lai, C., et al., 2012. Use of iron oxide nanomaterials in wastewater treatment: a review. Sci. Total Environ. 424, 1–10.
Xu, X., Song, W., Huang, D.G., Gao, B.Y., Sun, Y.Y., Yue, Q.Y., et al., 2015. Performance of novel biopolymer-based activated carbon and resin on phosphate elimination from stream. Colloids Surf. A 476, 68–75.
Yao, Y.J., Xu, F.F., Chen, M., Xu, Z.X., Zhu, Z.W., 2010. Adsorption behavior of methylene blue on carbon nanotubes. Bioresour. Technol. 101, 3040–3046.
Yao, S.H., Zhang, J.J., Shen, D.K., Xiao, R., Gu, S., Zhao, M., et al., 2016. Removal of Pb(II) from water by the activated carbon modified by nitric acid under microwave heating. J. Colloid Interface Sci. 463, 118–127.
Yurum, A., Kocabas-Atakli, Z.O., Sezen, M., Semiat, R., Yurum, Y., 2014. Fast deposition of porous iron oxide on activated carbon by microwave heating and arsenic (V) removal from water. Chem. Eng. J. 242, 321–332.
Zhai, Q.Q., Bo, T., Hu, G.X., 2011. High photoactive and visible-light responsive graphene/titanate nanotubes photocatalysts: preparation and characterization. J. Hazard. Mater. 198, 78–86.
Zhang, Y.R., Shen, S.L., Wang, S.Q., Huang, J., Su, P., Wang, Q.R., et al., 2014. A dual function magnetic nanomaterial modified with lysine for removal of organic dyes from water solution. Chem. Eng. J. 239, 250–256.
Zhang, Y.R., Su, P., Huang, J., Wang, Q.R., Zhao, B.X., 2015. A magnetic nanomaterial modified with poly-lysine for efficient removal of anionic dyes from water. Chem. Eng. J. 262, 313–318.
Zhou, X.X., Qu, X., Zhang, R., Bi, J.C., 2015. Study of the microtextural transformation of coal char during supercritical water activation. Fuel Process. Technol. 135, 195–202.